Monthly Notices
of the
ROYAL ASTRONOMICAL SOCIETY

MNRAS **481,** 1083–1096 (2018)
Advance Access publication 2018 August 25

doi:10.1093/mnras/sty2345

The scatter of the M dwarf mass–radius relationship

S. G. Parsons,[1]★ B. T. Gänsicke,[2] T. R. Marsh,[2] R. P. Ashley,[2] E. Breedt,[3] M. R. Burleigh,[4] C. M. Copperwheat,[5] V. S. Dhillon,[1,6] M. J. Green,[2] J. J. Hermes,[7]† P. Irawati,[8] P. Kerry,[1] S. P. Littlefair,[1] A. Rebassa-Mansergas,[9,10] D. I. Sahman,[1] M. R. Schreiber[11] and M. Zorotovic[11]

[1]*Department of Physics and Astronomy, University of Sheffield, Sheffield S3 7RH, UK*
[2]*Department of Physics, University of Warwick, Coventry CV4 7AL, UK*
[3]*Institute of Astronomy, University of Cambridge, Madingley Road, Cambridge CB3 0HA, UK*
[4]*Department of Physics and Astronomy, University of Leicester, Leicester LE1 7RH, UK*
[5]*Astrophysics Research Institute, Liverpool John Moores University, IC2, Liverpool Science Park L3 5RF, UK*
[6]*Instituto de Astrofísica de Canarias, Vía Lactea s/n, La Laguna, E-38205 Tenerife, Spain*
[7]*Department of Physics and Astronomy, University of North Carolina, Chapel Hill, NC 27599-3255, USA*
[8]*National Astronomical Research Institute of Thailand, 191 Siriphanich Bldg., Huay Kaew Road, Chiang Mai 50200, Thailand*
[9]*Departament de Física, Universitat Politècnica de Catalunya, c/Esteve Terrades 5, E-08860 Castelldefels, Spain*
[10]*Institut d'Estudis Espacials de Catalunya, Ed. Nexus-201, c/Gran Capità 2-4, E-08034 Barcelona, Spain*
[11]*Instituto de Física y Astronomía, Universidad de Valparaíso, Avenida Gran Bretana 1111, Valparaíso, 2360102, Chile*

Accepted 2018 August 23. Received 2018 August 22; in original form 2018 July 19

ABSTRACT

M dwarfs are prime targets in the hunt for habitable worlds around other stars. This is due to their abundance as well as their small radii and low masses and temperatures, which facilitate the detection of temperate, rocky planets in orbit around them. However, the fundamental properties of M dwarfs are difficult to constrain, often limiting our ability to characterize the planets they host. Here we test several theoretical relationships for M dwarfs by measuring 23 high-precision, model-independent masses and radii for M dwarfs in binaries with white dwarfs. We find a large scatter in the radii of these low-mass stars, with 25 per cent having radii consistent with theoretical models while the rest are up to 12 per cent overinflated. This scatter is seen in both partially and fully convective M dwarfs. No clear trend is seen between the overinflation and age or metallicity, but there are indications that the radii of slowly rotating M dwarfs are more consistent with predictions, albeit with a similar amount of scatter in the measurements compared to more rapidly rotating M dwarfs. The sample of M dwarfs in close binaries with white dwarfs appears indistinguishable from other M dwarf samples, implying that common envelope evolution has a negligible impact on their structure. We conclude that theoretical and empirical mass–radius relationships lack the precision and accuracy required to measure the fundamental parameters of M dwarfs well enough to determine the internal structure and bulk composition of the planets they host.

Key words: binaries: eclipsing – stars: fundamental parameters – stars: late-type.

1 INTRODUCTION

The discovery of a super-Earth orbiting the nearby (14.6 pc) M4.5 dwarf GJ 1214 (Charbonneau et al. 2009) via photometric follow-up of individual M dwarfs (Nutzman & Charbonneau 2008) and the recent radial-velocity detection of an Earth-mass planet at Proxima Centauri (Anglada-Escudé et al. 2016) demonstrate the enormous potential of planet searches focusing on low-mass stars, as their small radii and low masses substantially facilitate the discovery of smaller planets compared to planet searches at FGK stars. Consequently, M dwarfs are now key targets of many transit and radial surveys, e.g. NGTS (Wheatley et al. 2018), SPECULOOS (Delrez et al. 2018) and CARMENES (Reiners et al. 2018). In particular, TESS will survey the brightest and closest M dwarfs for transiting planets (Ricker et al. 2015), substantially increasing the number of known exoplanets orbiting low-mass stars (Ballard 2018). The identification of several temperate Earth-sized planets orbiting low-mass

★ E-mail: s.g.parsons@sheffield.ac.uk
† Hubble Fellow.

© 2018 The Author(s)
Published by Oxford University Press on behalf of the Royal Astronomical Society

Downloaded from https://academic.oup.com/mnras/article/481/1/1083/5079656 by guest on 18 November 2024

stars (Dittmann et al. 2017a; Gillon et al. 2016, 2017), combined with the fact that M dwarfs are the most numerous stars in the Milky Way, has led to considerable interest in the habitability of these worlds (Seager 2013; Kopparapu et al. 2017; Wandel 2018).

A fundamental limitation in the characterization of exoplanets is that the derived bulk parameters, including masses, radii, and densities, require accurate knowledge of the planet host properties. Accurate planet radii and masses (which require accurate stellar radii and masses) are required to gauge insight into their internal structure and bulk composition. Valencia, Sasselov & O'Connell (2007) argued that planet radius measurements to better than 5 per cent and mass measurements to better than 10 per cent are necessary to distinguish between rocky and icy bulk composition, and even then, details of the interior composition are model-dependent (Rogers & Seager 2010; Dorn et al. 2015).

It has been well established that the measured radii of low-mass stars (<0.6 $M_{\odot}$) are larger than predicted by evolutionary models, by up to 10–20 per cent (López-Morales & Ribas 2005). This is thought to be caused by the fact that virtually all precise mass–radius measurements of low-mass stars come from stars in close binaries.[1] These stars are tidally locked and are hence rapid rotators and magnetically active. This activity is thought to lead to a cooler and larger star (Morales, Ribas & Jordi 2008) and can therefore explain the overinflation, an idea supported by the fact that the interferometrically measured radii of isolated, inactive low-mass stars appear more consistent with evolutionary models (Demory et al. 2009). Magnetic activity can also explain the 14 per cent larger radii of young low-mass stars in the Pleiades cluster (Jackson, Deliyannis & Jeffries 2018). However, the reality is more complicated than this, as there are several relatively inactive nearby low-mass stars with interferometric radii more than 15 per cent too large (Berger et al. 2006) and there are stars in long period, slowly rotating binaries that are also oversized (Doyle et al. 2011; Irwin et al. 2011). Conversely, there are rapidly rotating low-mass stars in close binaries that have radii consistent with evolutionary models (Blake et al. 2008), and some binaries where one component has a consistent radius and its companion is oversized (Kraus et al. 2017), implying that there are a number of different factors that affect the overinflation beyond enhanced magnetic activity. Recent work from Kesseli et al. (2018) also shows that neither rotation nor binarity is responsible for the inflated radii of low-mass stars.

The number of precisely characterized low-mass stars is still low, due mainly to their faintness. Pairs of eclipsing low-mass stars are still the benchmark systems for such measurements (López-Morales 2007), but few are known and fewer still are bright enough to be studied at high precision. Moreover, the effects of starspots on both stars make modelling their light curves complex. Low-mass stars in eclipsing binaries with more massive solar-type stars are more numerous and brighter, but the large brightness contrast between the two stars often means that the M star is essentially undetectable spectroscopically, meaning that not only are these single-lined binaries (making them less ideal for testing evolutionary models), but precise temperature measurements for the M star are extremely challenging. Interferometric studies of isolated low-mass stars can yield very precise radii, but lack the mass precision provided by binary systems and are limited to a few nearby bright stars.

One type of system that is often overlooked is low-mass stars in detached eclipsing binaries with white dwarfs. More than 3000 white dwarf plus main-sequence star binaries are known (Rebassa-Mansergas et al. 2016a; Ren et al. 2018), including more than 70 eclipsing systems (Parsons et al. 2015). The small size of the white dwarf (roughly Earth sized) results in very sharp eclipse features that can be used to measure radii to very high precisions (1–2 per cent in the best cases; e.g. Parsons et al. 2010). Moreover, in most cases both the white dwarf and low-mass star are visible in optical spectra, making these double-lined binaries. Low-mass stars are roughly 10 times larger than white dwarfs, meaning that the eclipse of the white dwarf is total and a clean spectrum of the low-mass star can be obtained without contamination from the white dwarf. Finally, the cooling of white dwarfs is well understood, making them ideal objects for constraining the ages of their low-mass stellar companions.

It should be noted that these systems have experienced a brief common envelope phase in their past evolution, when the progenitor star of the white dwarf evolved off the main-sequence. During the common envelope phase (or rather shortly prior to it) mass was transferred to the low-mass star. However, this phase is extremely short (10^3–10^4 yr) compared to the thermal time-scale of a low-mass star (10^8–10^9 yr) and so has a negligible effect on the star. The common envelope itself possesses much higher specific entropy than the surface of the M dwarf, meaning that the star is thermally isolated from the common envelope and hence essentially no accretion takes place (Hjellming & Taam 1991).

In this paper we present 16 high-precision mass and radius measurements for M dwarfs in eclipsing binaries with white dwarfs. Along with another seven previously studied systems we also determine the effective temperatures, metallicities and ages of these stars and compare these to the predictions of evolutionary models.

2 OBSERVATIONS AND THEIR REDUCTION

High cadence eclipse light curves for all our targets were obtained with the high-speed frame-transfer cameras ULTRACAM (Dhillon et al. 2007) on the 8.2-m VLT and 3.5-m NTT in Chile and 4.2-m WHT on La Palma and ULTRASPEC (Dhillon et al. 2014) on the 2.4-m TNT in Thailand. Intermediate resolution optical and near-infrared spectroscopy was obtained using the X-shooter spectrograph (Vernet et al. 2011) on the VLT, including observations of several M dwarf spectral standard stars, which are detailed in Table 1. All of these observations and their reductions are detailed in Parsons et al. (2017). In addition to these data we also obtained a single X-shooter spectrum of the system RR Cae on 2017 August 30. This was reduced in an identical manner to the other X-shooter data. We plot the X-shooter VIS arm spectra taken during the eclipse of the white dwarf (i.e. of the M dwarf component only) in Fig. 1.

3 STELLAR PARAMETERS

3.1 Masses and radii

A detailed account of how we measured the masses and radii of each star in all our binaries is given in Parsons et al. (2017). In brief, radial velocity semi-amplitudes were measured from our spectra and combined with fits to the eclipse light curves (see Fig. 2). However, fits to the white dwarf eclipse alone are degenerate (they only give

[1] While accurate parallaxes help to constrain stellar radii of single stars if their effective temperature can be empirically constrained, their masses require additional information, such as an independent measure of their surface gravity from planet transits (Southworth, Wheatley & Sams 2007; Stassun, Collins & Gaudi 2017), or from their granulation-driven variability (Stassun et al. 2018) and hence remain limited in their accuracy.

Downloaded from https://academic.oup.com/mnras/article/481/1/1083/5079656 by guest on 18 November 2024

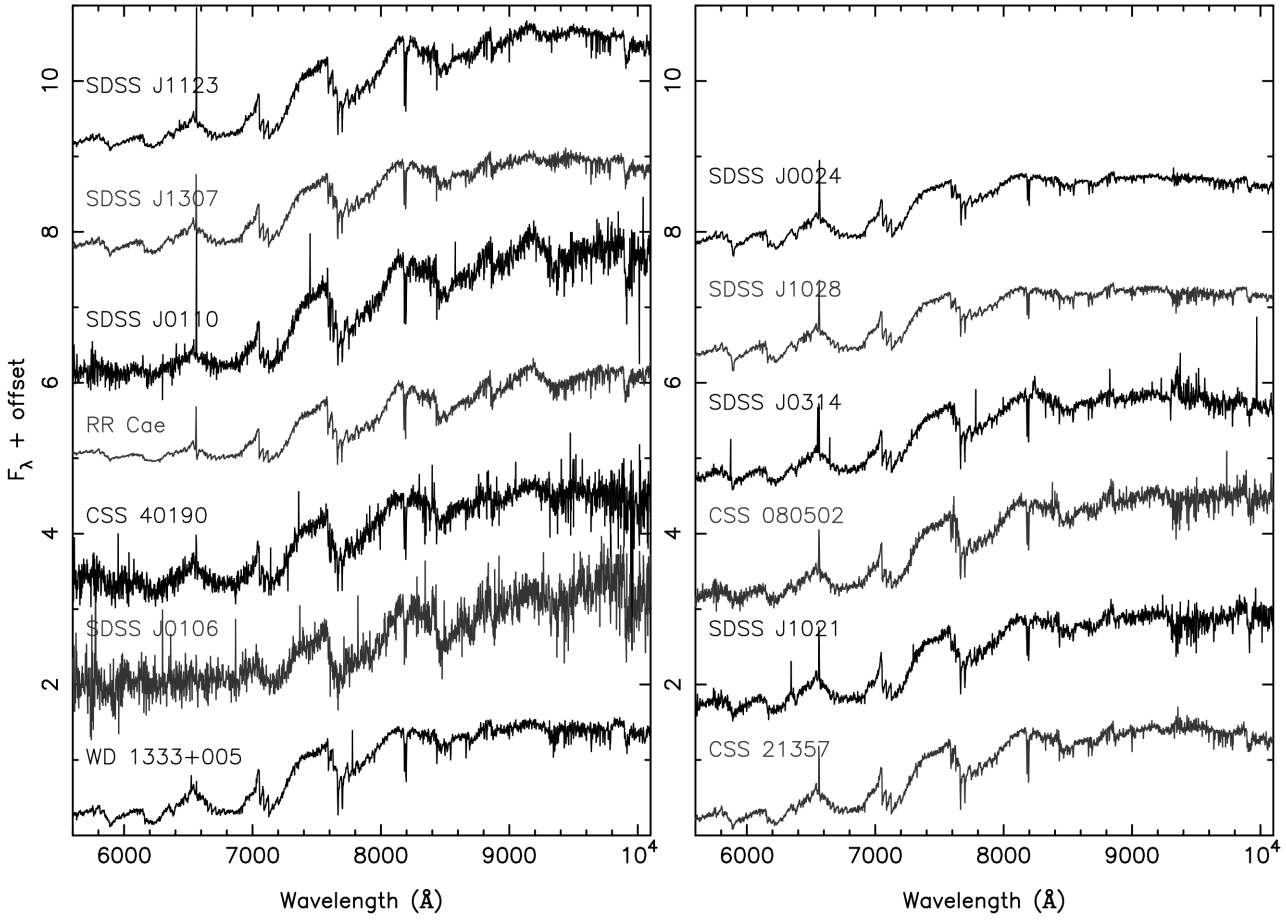

Figure 1. X-shooter VIS arm spectra of the M dwarfs in our binaries ordered from least massive (bottom-left) to most massive (top-right). These spectra were all obtained during the eclipse of the white dwarf and so only the M dwarf component is visible. The spectra have been binned by a factor of 10 for clarity. We do not plot the very noisy in-eclipse spectra of CSS 09704, SDSS J1329+1230 or SDSS J2235+1428.

the relationship between the two radii as a function of inclination) and an additional piece of information is required to determine the inclination and hence solve for the physical parameters. This additional information could be: (1) the rotational broadening of the M star, (2) the gravitational redshift of the white dwarf or, (3) the depth of the secondary eclipse (the transit of the white dwarf in front of the M star). Generally, each system requires a different technique and we refer readers to Parsons et al. (2017) for details of how each individual system was solved. The masses and radii of the M dwarfs in our sample are listed in Table 2 and shown in Fig. 3. Note that many of these M stars are tidally distorted by their white dwarf companions, therefore, the quoted radii are the volume-averaged radii of the stars, which is most closely representative of the radii the stars would have if they were isolated.

3.2 Spectral types

The spectral types of the M dwarfs in our sample were determined using template fitting. We observed a number of spectral type template stars with X-shooter using an identical instrumental setup to our main science observations. These template stars are detailed in Table 1. We used the spectra of our targets taken during the eclipse of the white dwarf and fitted the K I 7699 Å, Na I 8183/8194 Å and K I 1.252 μm lines with each template spectrum. We artificially broadened the lines of the template spectra to fit the observed lines, taking into account any additional smearing of the lines from the velocity shift during the exposure (see Marsh, Robinson & Wood 1994, for details of this method). We applied a high-pass filter to both the observed and broadened template spectra before comparing them in order to prevent the continuum dominating the fit. The best-fitting template then yields both the rotational broadening of the M star and its spectral type.

In five cases the in-eclipse spectrum of the M dwarf was very poor and the template fitting technique was not possible. In these cases we constrained the spectral type of the M star using its $r - i$ colour measured from the eclipse light curves and the relations of West, Walkowicz & Hawley (2005). The spectral types of all our M dwarfs are listed in Table 2.

3.3 Effective temperatures

Effective temperatures were determined by comparing our in-eclipse M dwarf spectra with a library of synthetic spectra. We used the BT-Settl model spectra from Allard et al. (2013), which are suitable for the low temperatures of M dwarfs. The surface gravity was fixed to the nearest model based on the measured mass and radius (either $\log g = 4.5$ or 5.0). The metallicity was fixed at solar ([Fe/H] = 0) which is the closest model value to our measured metallicities (see Section 3.4), and no α-element enhancement. We then used a grid of temperatures from 2300 to 4500 K in steps of

Downloaded from https://academic.oup.com/mnras/article/481/1/1083/5079656 by guest on 18 November 2024

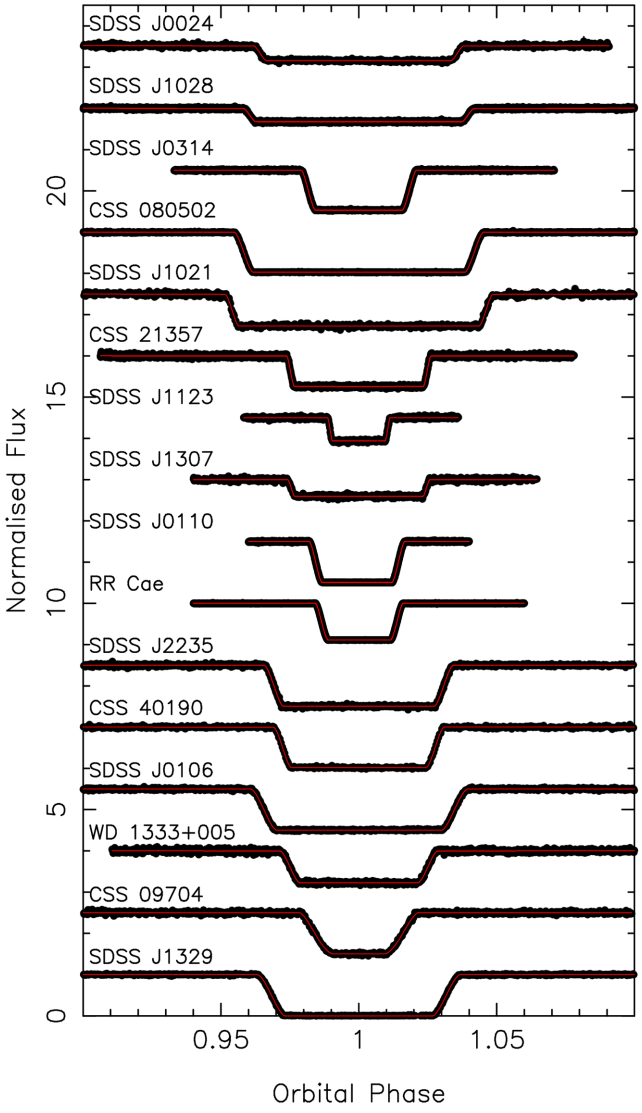

Figure 2. Light curves of the eclipse of the white dwarf in our binaries with model fits overplotted in red. Light curves are ordered from the least massive (bottom) to most massive (top) M star and are offset vertically by 1.5. The light curves shown are in the g' band or the *KG*5 band (for WD 1333+005, SDSS J1307+2156, SDSS J1123 − 1155, CSS 21357 and SDSS J1028+0931). The *KG*5 filter is a broad-band ($u' + g' + r'$) filter [see Hardy et al. (2017) for details].

100 K. Each model was first degraded to match the resolution of our X-shooter spectra and then rotationally broadened based on the measured $v \sin i$ values. Models were compared over the X-shooter VIS arm wavelengths (5600–10 000 Å) excluding the region around the H α line (6500–6650 Å); note that our spectra were corrected for telluric features (using observations of telluric standard stars taken shortly before or after our science spectra). For each object the best-fitting model was determined via χ^2 minimization (see Table 2 for the results).

In the case of objects with poor signal-to-noise ratio spectra the effective temperature was instead determined by fitting the observed spectral energy distribution (SED) of the binary. A model white dwarf spectrum was first removed from the SED based on the fitted white dwarf parameters (see Parsons et al. 2017 for the white dwarf parameters), then the SED was fitted using the virtual observatory SED analyzer (VOSA; Bayo et al. 2008). These values are also listed in Table 2 and generally have a larger uncertainty than the spectral fits.

We also applied these fits to all of the previously published objects listed in Table 2 using the data presented in those studies.

3.4 Metallicities

Metallicities of M dwarfs are notoriously difficult to measure and generally rely on empirical relations derived from M dwarfs in binaries with higher mass F, G and K stars. To measure the metallicities of our stars we used the semi-empirical method outlined in Newton et al. (2014), which relies solely on the equivalent width of the Na I 2.205/2.209 μm absorption doublet, which is covered in our X-shooter data. This method has been shown to give [Fe/H] values to (at best) a precision of up to 0.12 dex for M1–M5 dwarfs. It has yielded reliable metallicities in other white dwarf plus M dwarf binaries using similar X-shooter data (Rebassa-Mansergas et al. 2016b).

Our measured [Fe/H] values are detailed in Table 2 for those M dwarfs with spectral types between M1 and M5. In several cases the quality of the near-infrared spectrum was insufficient to give reliable equivalent width measurements for the sodium doublet.

3.5 Ages

Ages are extremely difficult to measure for low-mass main-sequence stars. While the ages of more massive solar-type stars can be constrained using chromospheric activity indicators (e.g. Soderblom, Duncan & Johnson 1991), isochrone fitting (Serenelli et al. 2013) or gyrochronology (Barnes 2010), the situation is more complicated for M dwarfs and most reliable measurements come from low-mass stars in clusters. Given that the radius of a low-mass star can change as much as 5 per cent between 1 and 10 Gyr (Baraffe et al. 2015), it is important to compare our measured radii with theoretical models of the right age. Fortunately, the white dwarf companions to our M dwarfs can be used to constrain the ages of our stars.

Since the white dwarf parameters are known to high precision, their cooling ages can be calculated to a few per cent. Normally an initial-to-final mass relationship is then used to estimate the mass of the progenitor star of the white dwarf (e.g. Catalán et al. 2008) and determine the main-sequence lifetime and therefore establish the total age of the object. However, in the case of close binary systems such as those presented here, this approach is not appropriate because the evolution of the white dwarf progenitor was truncated by its low-mass companion (due to a common envelope phase) and hence an initial-to-final mass relation would underpredict the progenitor mass and overpredict the total age. For these kinds of objects it is necessary to properly reconstruct the evolutionary history of each system, which we did following the algorithm described in detail by Zorotovic, Schreiber & Gänsicke (2011, section 3.2). For a proper estimation of the errors, we have randomly generated a Gaussian distribution for the white dwarf masses for each system, centred on the observed mass and with a standard deviation that corresponds to the measured error, as listed in Parsons et al. (2017). We have then computed the cooling ages and periods just after the common envelope phase for the 1000 masses for each system assuming disrupted magnetic braking (Rappaport, Verbunt & Joss 1983). These parameters were used to reconstruct their evolutionary histories assuming a common envelope efficiency in the range of 0.2–0.3 and no contributions from recombination energy. The

Downloaded from https://academic.oup.com/mnras/article/481/1/1083/5079656 by guest on 18 November 2024

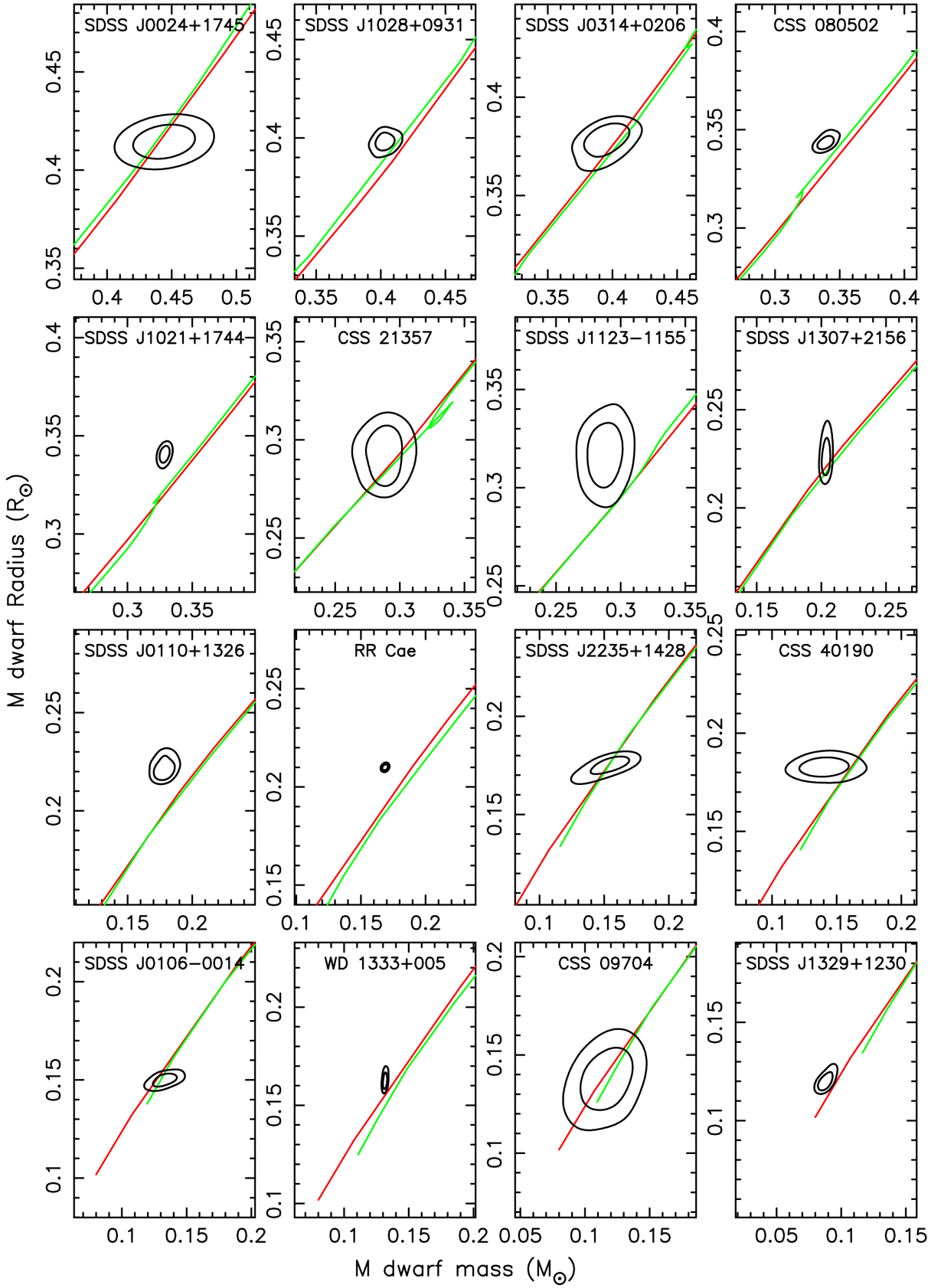

Figure 3. Constraints on the masses and radii (volume averaged) of the M dwarfs in all our systems, shown as contours (68 and 95 percentile regions). Red lines show the Baraffe et al. (2015) theoretical mass–radius relationship using the model with the closest match in age. Green lines show the Dotter et al. (2008) relationship with matching ages and metallicities (solar metallicity is used when we have no constraints.). All plots are on the same scale and centred on the mean mass–radius value for each M dwarf and run from most massive (top-left) to least massive (bottom-right).

Downloaded from https://academic.oup.com/mnras/article/481/1/1083/5079656 by guest on 18 November 2024

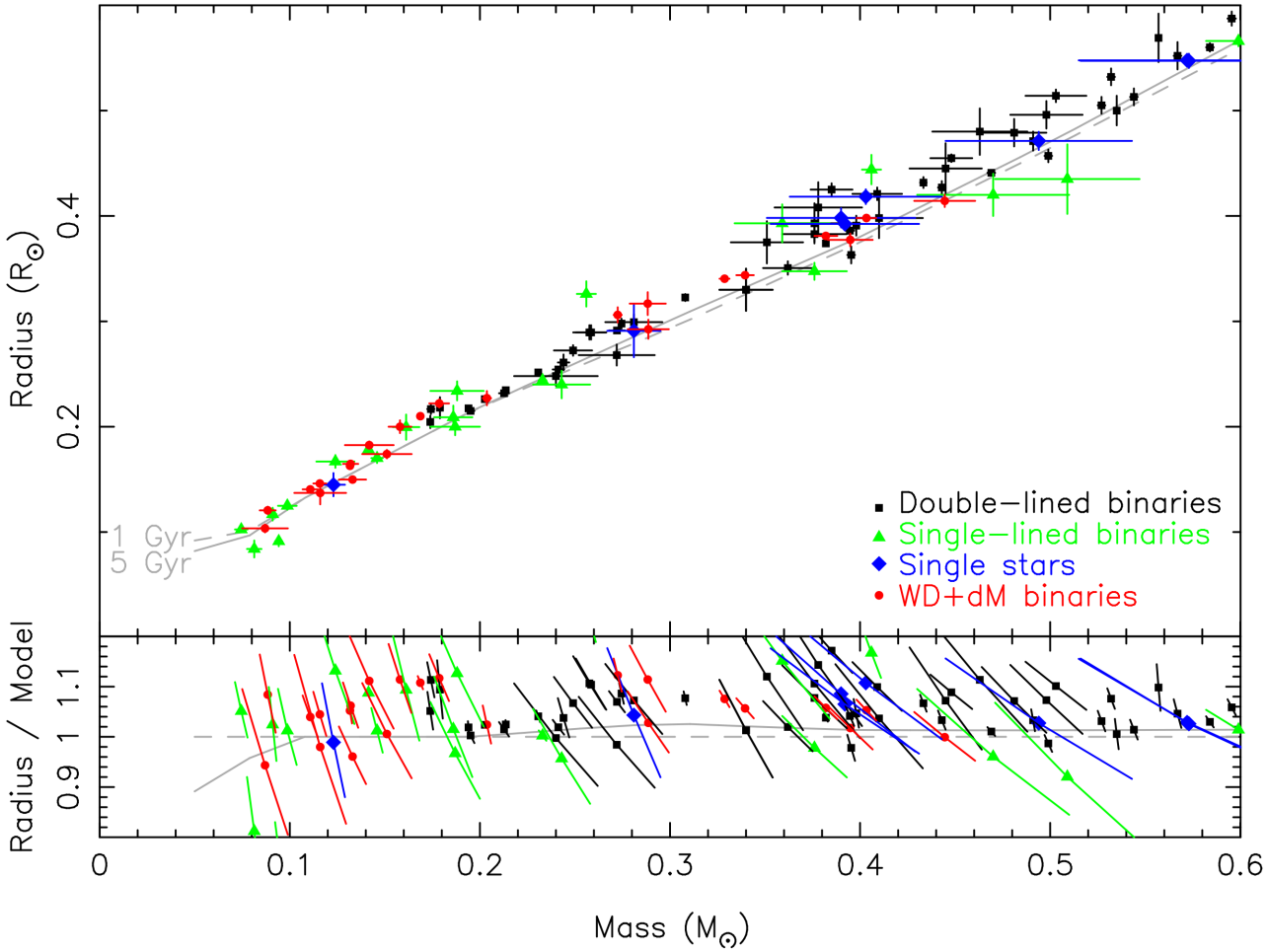

Figure 4. Mass–radius plot for low-mass stars (with mass and radius uncertainties of less than 10 per cent). The type of system that the measurement came from is indicated by the different colours and symbols and all are detailed in either Table 2 (red points) or the Appendix (all other points). Also shown are the theoretical mass–radius tracks from Baraffe et al. (2003, 2015).

derived total age of each system is listed in Table 2, corresponding to the median of all the possible solutions for each system, while the errors represent the 34 percentile regions on each side of the median. We have also verified that the errors in the effective temperatures of the white dwarfs are negligible compared to the effect of the errors on the masses.

4 COMPARISON TO THEORETICAL MODELS

4.1 The mass–radius relation

Table 2 lists all of our measurements as well as those of other M dwarfs in eclipsing binaries with white dwarfs. The masses and radii of these objects are shown in Fig. 4 along with other precise mass–radius measurements collected from other sources (these are detailed in Table A1 in the Appendix). Both Figs 3 and 4 show large amounts of scatter in the measured radii of low-mass stars relative to theoretical predictions. In some cases the measured radii are consistent with models, while in others the radii are more than 10 per cent larger than expected. For example, the white dwarf plus M dwarf binaries CSS 21357 and SDSS J1123 − 1155 have M dwarfs with essentially identical masses (0.289 ± 0.011 $M_\odot$ and 0.288 ± 0.009 $M_\odot$) but their radii differ from each other by 9 per cent, with CSS 21357 having a radius consistent with models while SDSS J1123 − 1155 is substantially oversized. This trend has been seen before, for example the eclipsing binary PTFEB132.707 + 19.810 contains two low-mass stars, one of which has a radius consistent with evolutionary models, while the other is 20 per cent larger than expected (Kraus et al. 2017).

On average our measured radii are 6.2 per cent larger than predicted, although the scatter on this value is substantial (4.8 per cent), indicating that this is not a systematic offset. This overinflation is seen in both partially convective stars (4.0 ± 2.5 per cent oversized) and fully convective stars (7.1 ± 5.1 per cent oversized). Given that all of our stars are tidally locked in short period ($P_{\rm orb} < 1$ d) binaries it is clear that this overinflation cannot be solely due to rapid rotation and enhanced magnetic activity. Taking all of the measurements shown in Fig. 4 (i.e. all the values listed in Table 2 and the Appendix) gives an average overinflation of 5 per cent for both partially and fully convective stars, but with a scatter of 5 per cent and little difference between the different types of system. No clear difference is seen between the measured radii of M dwarfs from different sources, confirming that the structure of M dwarfs in close binaries with white dwarfs is not affected by common envelope evolution.

Downloaded from https://academic.oup.com/mnras/article/481/1/1083/5079656 by guest on 18 November 2024

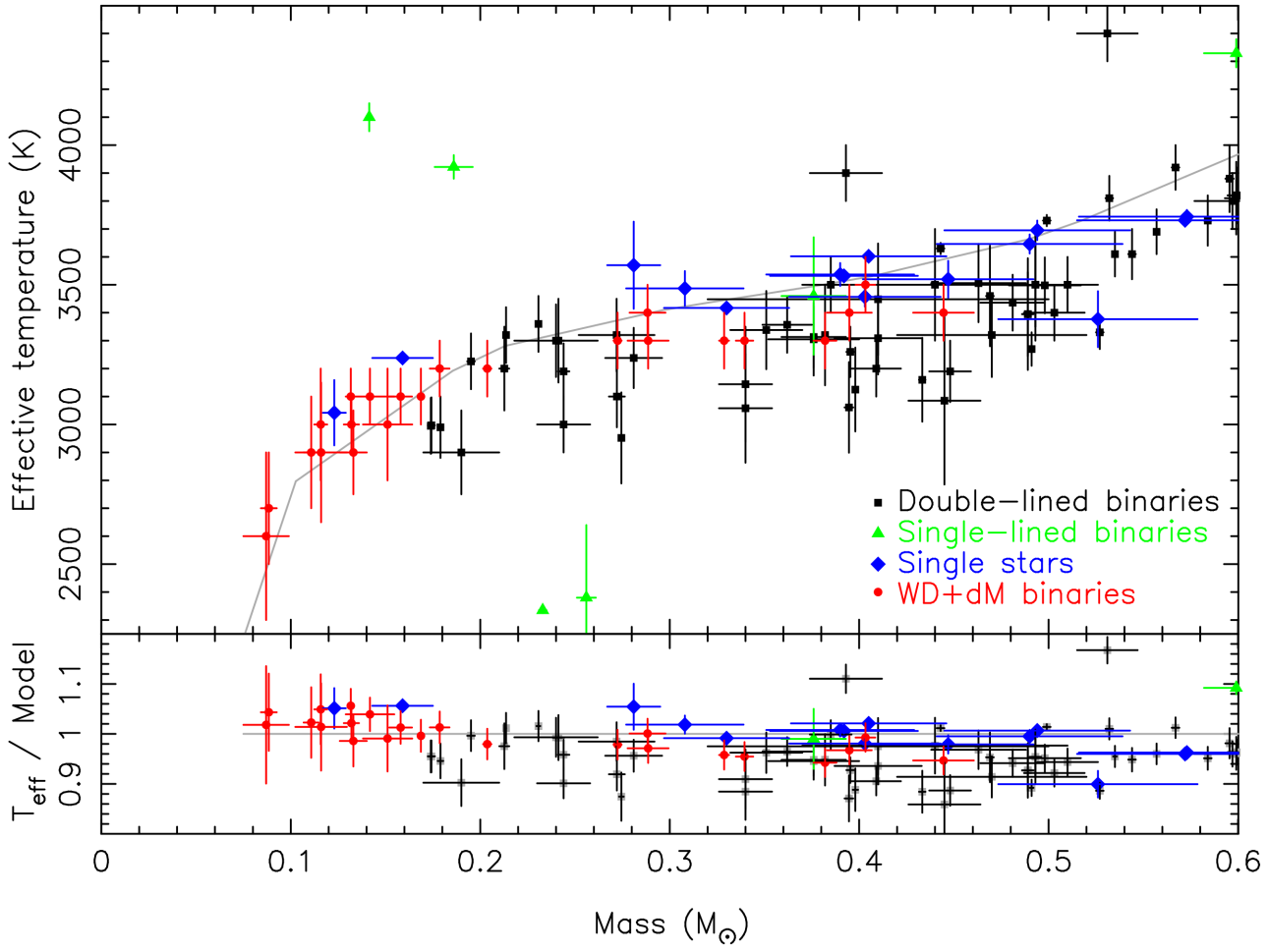

Figure 5. Mass–effective temperature plot for low-mass stars. The type of system that the measurement came from is indicated by the different colours and symbols and all are detailed in either Table 2 or the Appendix. Also shown are the theoretical tracks from Baraffe et al. (2003, 2015) for an age of 1 Gyr.

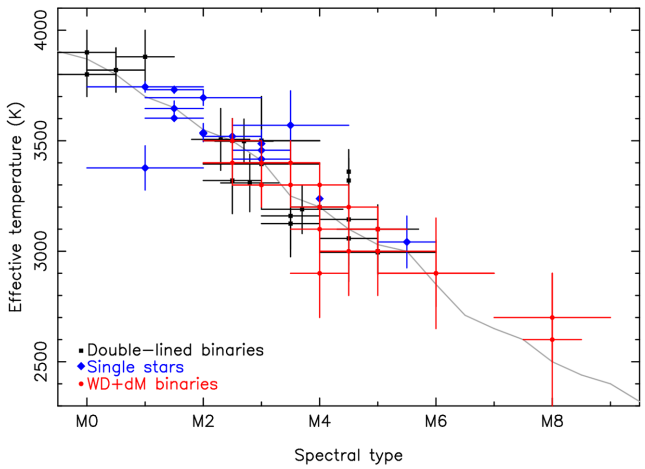

Figure 6. The spectral type–$T_{\rm eff}$ relation for M dwarfs. The type of system that the measurement came from is indicated by the different colours and symbols and all are detailed in Table 2 or the Appendix. The grey line is the observed relation from Pecaut & Mamajek (2013).

4.2 The mass–$T_{\rm eff}$ relation

Fig. 5 shows the measured temperatures of our M dwarfs as a function of mass. Our systems mostly populate the low temperature end of the plot, which is a region with few previous measurements. Interestingly, our temperature measurements for the very low mass stars ($<0.2\,{\rm M}_{\odot}$) are in agreement with theoretical predictions. The stars more massive than this are all cooler than predicted by 100–200 K, a trend seen in many stars in this mass regime (López-Morales 2007). On average, fully convective stars are only 50 K cooler than expected, while partially convective stars are 150 K cooler than theoretical models predict; however, there is not a clear boundary between the two at $0.35\,{\rm M}_{\odot}$, rather the agreement with theoretical models becomes better at lower masses. This behaviour is expected since the luminosity of fully convective stars is set by the conditions in their very outermost layers (Sirotkin & Kim 2010) and therefore their effective temperatures should change little on expansion, as opposed to partially convective stars.

Five per cent of systems are significant outliers with temperatures more than ∼500 K hotter or cooler than models predict. It is unclear why the temperatures of these specific objects are so discrepant, although we note that the majority of these highly discrepant measurements are from single-lined systems.

Downloaded from https://academic.oup.com/mnras/article/481/1/1083/5079656 by guest on 18 November 2024

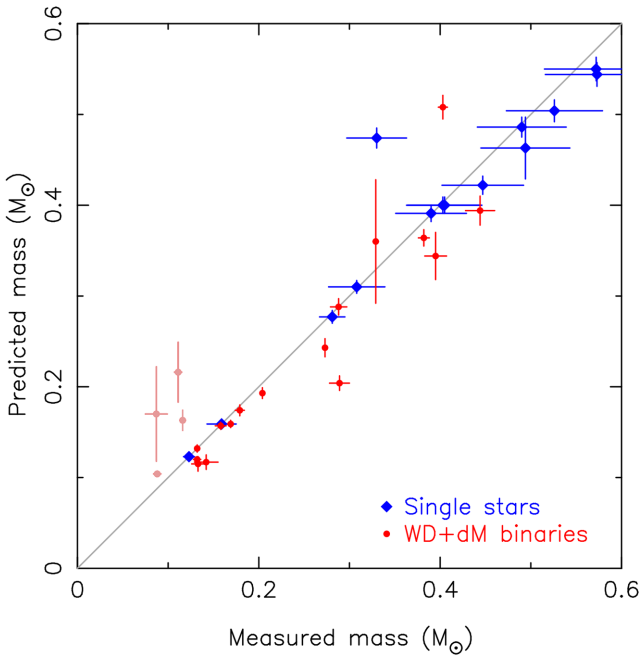

Figure 7. The measured masses of M dwarfs compared to those derived using the empirical mass–M_{K_s} relation from Mann et al. (in preparation). Faded red points are binaries where the white dwarf still contributes a substantial amount of the flux in the K_s band and therefore may not have reliable predicted masses.

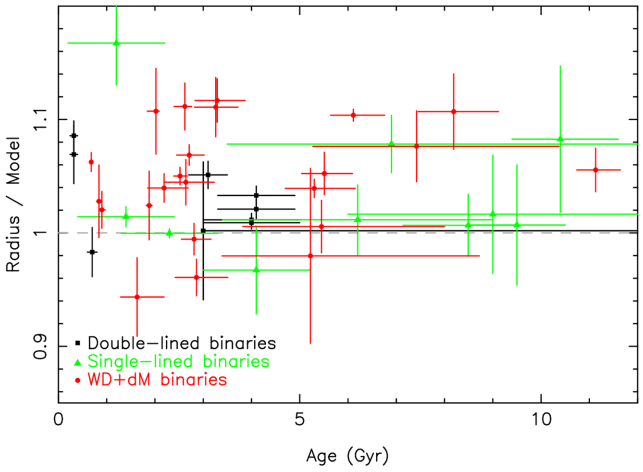

Figure 8. The overinflation of M dwarfs as a function of their ages. Measured radii were compared to the closest Baraffe et al. (2015) model in age.

4.3 The spectral type–$T_{\rm eff}$ relation

Fig. 6 shows the spectral type–$T_{\rm eff}$ relation using the stars in the sample with spectral type and temperature measurements listed in Table 2 and the Appendix. Our new measurements show excellent agreement with the empirical relation of Pecaut & Mamajek (2013) (which uses single stars), with all our measurements consistent to within 2 sigma.

4.4 The mass–M_{K_s} relation

We determined the absolute K_s- band magnitudes of the M dwarfs in our binaries using their 2MASS measurements (or UKIDSS for the

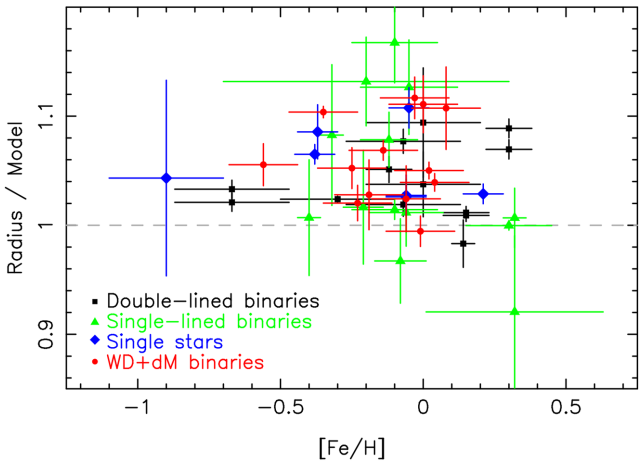

Figure 9. The overinflation of M dwarfs as a function of their metallicity. Radii were compared to solar metallicity models from Baraffe et al. (2015).

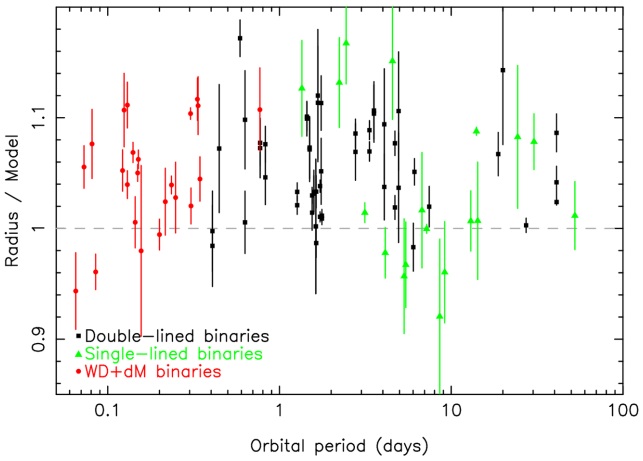

Figure 10. The overinflation of M dwarfs as a function of their orbital period. Note that many stars in systems with periods longer than a few days are not synchronously rotating (usually rotating slower than the binary period) and generally have moderately eccentric orbits.

Table 1. M dwarf template stars used in this study.

Name	SpT	V	K
LP 887 − 70	M1.0V	11.00	7.12
LP 905 − 56	M1.5V	11.22	6.99
GJ 2066	M2.0V	10.09	5.77
GJ 588	M2.5V	9.31	4.76
GJ 812	M3.0V	11.92	7.06
GJ 849	M3.5V	10.37	5.59
GJ 876	M4.0V	10.19	5.01
GJ 3366	M4.5V	14.54	9.18
GJ 2045	M5.0V	15.36	9.37
V645 Cen	M5.5V	11.13	4.38
Wolf 359	M6.0V	13.51	6.08
LP 731 − 47	M6.5V	17.53	10.79
2MASS J01273195 − 3140031	M7.0V	20.40	11.66
LHS 2021	M7.5V	19.06	10.76
2MASS J10481463−3956062	M8.0V	17.53	8.45

Downloaded from https://academic.oup.com/mnras/article/481/1/1083/5079656 by guest on 18 November 2024

Table 2. M dwarf mass–radius measurements obtained from detached, eclipsing binaries with white dwarfs. All temperature, metallicity and age measurements are from this paper. π is the *Gaia* DR2 parallax. Effective temperatures indicated with a † symbol were determined from SED fitting rather than fitting with synthetic spectra. Spectral types indicated with a asterisk (∗) symbol were determined from the in-eclipse $r - i$ colour instead of template fitting. References for the other measurements are given in the final column: (1) This paper; (2) Parsons et al. (2016); (3) Parsons et al. (2012b); (4) Pyrzas et al. (2012); (5) Parsons et al. (2012c); (6) Parsons et al. (2010) and (7) Parsons et al. (2012a).

Object	g mag	P_{orb} (h)	Mass ($M_\odot$)	Radius ($R_\odot$)	T_{eff} (K)	[Fe/H] (dex)	Age (Gyr)	Sp type	π (mas)	Ref
SDSS J0024 + 1745	18.71	4.801	0.444 ± 0.016	0.414 ± 0.006	3400 ± 100	-0.01 ± 0.12	$2.81^{+0.35}_{-0.26}$	M2.5 ± 0.5	3.70 ± 0.12	1
SDSS J1028 + 0931	16.40	5.641	0.403 ± 0.005	0.398 ± 0.003	3500 ± 100	$+0.04 \pm 0.12$	$5.30^{+0.85}_{-0.60}$	M2.5 ± 0.5	5.70 ± 0.06	1
SDSS J0314 + 0206	16.95	7.327	0.395 ± 0.012	0.377 ± 0.006	3400 ± 100	-0.23 ± 0.12	$0.90^{+0.07}_{-0.06}$	M3.0 ± 1.0	2.33 ± 0.13	1
QS Vir	14.66	3.618	0.382 ± 0.006	0.381 ± 0.003	3300 ± 100	-	$0.68^{+0.02}_{-0.01}$	M3.0 ± 0.5	19.96 ± 0.06	2
CSS 080502	17.08	3.587	0.340 ± 0.005	0.344 ± 0.003	3300 ± 100	$+0.02 \pm 0.12$	$2.52^{+0.15}_{-0.13}$	M3.5 ± 0.5	-	1
SDSS J1021 + 1744	19.51	3.369	0.329 ± 0.003	0.340 ± 0.003	3300 ± 100	-0.14 ± 0.12	$2.71^{+0.31}_{-0.26}$	M3.0 ± 0.5	2.28 ± 0.44	1
CSS 21357	17.29	5.962	0.289 ± 0.011	0.293 ± 0.009	3300 ± 100	-0.19 ± 0.12	$0.84^{+0.06}_{-0.05}$	M3.0 ± 0.5	6.08 ± 0.13	1
SDSS J1123 − 1155	17.99	18.459	0.288 ± 0.009	0.317 ± 0.011	3400 ± 100	$+0.08 \pm 0.12$	$2.02^{+0.07}_{-0.18}$	M3.5 ± 0.5	6.32 ± 0.10	1
SDSS J1212 − 0123	16.77	8.061	0.273 ± 0.002	0.306 ± 0.007	3300 ± 100	$+0.00 \pm 0.12$	$3.26^{+0.46}_{-0.44}$	M4.0 ± 0.5	4.80 ± 0.11	3
SDSS J1307 + 2156	18.25	5.192	0.204 ± 0.002	0.227 ± 0.007	3200 ± 100	-0.06 ± 0.12	$1.88^{+0.06}_{-0.06}$	M4.0 ± 0.5	9.43 ± 0.08	1
SDSS J0110 + 1326	16.53	7.984	0.179 ± 0.005	0.222 ± 0.004	3200 ± 100	-0.03 ± 0.12	$3.29^{+0.58}_{-0.46}$	M4.5 ± 0.5	3.60 ± 0.10	1
RR Cae	14.57	7.289	0.169 ± 0.001	0.210 ± 0.001	3100 ± 100	-0.35 ± 0.12	$6.11^{+0.65}_{-0.47}$	M4.0 ± 0.5	47.16 ± 0.02	1
SDSS J1210 + 3347	16.94	2.988	0.158 ± 0.006	0.200 ± 0.006	3100 ± 100	-	$8.19^{+0.93}_{-0.74}$	M5.0 ± 0.5	21.69 ± 0.08	4
SDSS J2235 + 1428	18.59	3.467	0.151 ± 0.013	0.174 ± 0.004	$3000 \pm 200^\dagger$	-	$5.45^{+2.55}_{-1.63}$	M5.0 ± 1.0*	-	1
CSS 40190	18.16	3.123	0.142 ± 0.013	0.183 ± 0.003	3100 ± 100	-	$2.62^{+0.14}_{-0.22}$	M5.0 ± 0.5	3.51 ± 0.29	1
SDSS J0106 − 0014	18.14	2.040	0.133 ± 0.007	0.150 ± 0.002	$2900 \pm 150^\dagger$	-	$2.86^{+0.65}_{-0.44}$	M6.0 ± 1.0*	3.16 ± 0.26	1
SDSS J0138 − 0016	18.84	1.746	0.132 ± 0.004	0.165 ± 0.003	3000 ± 100	-0.56 ± 0.12	$11.13^{+0.51}_{-0.39}$	M5.0 ± 0.5	20.09 ± 0.33	5
WD 1333+005	17.41	2.927	0.132 ± 0.001	0.163 ± 0.003	3100 ± 100	-0.25 ± 0.12	$5.51^{+0.58}_{-0.47}$	M5.0 ± 0.5	10.63 ± 0.12	1
GK Vir	16.81	8.264	0.116 ± 0.003	0.146 ± 0.003	$3000 \pm 200^\dagger$	-	$2.64^{+0.59}_{-0.45}$	M4.5 ± 0.5	2.11 ± 0.13	3
CSS 09704	18.41	3.756	0.116 ± 0.014	0.137 ± 0.011	$2900 \pm 250^\dagger$	-	$5.22^{+3.50}_{-1.83}$	M6.0 ± 1.0*	1.93 ± 0.40	1
NN Ser	16.43	3.122	0.111 ± 0.004	0.141 ± 0.002	$2900 \pm 200^\dagger$	-	$2.19^{+0.50}_{-0.34}$	M4.0 ± 0.5	1.92 ± 0.10	6
SDSS J1329 + 1230	17.26	1.943	0.088 ± 0.004	0.121 ± 0.004	$2700 \pm 200^\dagger$	-	$7.42^{+2.95}_{-2.15}$	M8.0 ± 1.0*	4.57 ± 0.14	1
SDSS J0857 + 0342	17.95	1.562	0.087 ± 0.012	0.104 ± 0.004	$2600 \pm 300^\dagger$	-	$1.63^{+0.56}_{-0.34}$	M8.0 ± 0.5*	0.99 ± 0.30	7

fainter objects) and parallaxes from *Gaia* data release 2 (Gaia Collaboration et al. 2018), and list them in Table 2. Two of our binaries lack reliable *Gaia* parallaxes (CSS 080502 and SDSS J2235+1428), while one target has no near-infrared magnitude measurements (CSS 09704), so we exclude these three targets from our subsequent analysis. The remaining targets all have high-precision *Gaia* parallaxes (parallax/error>10), so their distances can be determined by simple parallax inversion without significant loss of accuracy (Bailer-Jones et al. 2018) and hence absolute K_s- band magnitudes can be derived. We used these values and the empirical mass–M_{K_s} relationship from Mann et al. (in preparation) to estimate the masses of our M dwarfs[2] and compared these to our measured values. Fig. 7 shows the difference between the measured and predicted values for the M dwarfs in our binaries as well as the single stars listed in the Appendix. We do not include M dwarfs in either double- or single-lined binaries since measuring the K_s magnitude for the M dwarf alone is difficult in these binaries due to contamination from their companion stars. This is one of the advantages of using white dwarf–M dwarf binaries since in the majority of cases the M dwarf completely dominates the flux in the K_s band. However, this is not always the case; in systems with very low mass M dwarfs and/or extremely hot white dwarfs a significant amount of the K_s- band flux originates from the white dwarf. We have highlighted these systems in Fig. 7 and the predicted masses of these objects has clearly been overestimated – these points should be disregarded when comparing values in Fig. 7. In-eclipse K_s- band measurements would remove this issue since the white dwarf contribution would be obscured.

The mass–luminosity relationship systematically underpredicts our measured masses by 5–10 per cent. Single stars are more consistent, although their masses are also slightly underpredicted (albeit with larger mass errors). This may be due to the enhanced number of star spots on M dwarfs in our close binaries, which would lead to slightly fainter stars and therefore an under prediction of their masses, although this should not be a large effect in the K_s band.

4.5 The effect of age

The radii of low-mass stars change slowly over time, most notably in the first billion years as they evolve on to the main sequence. Once on the main-sequence however, the radii of M dwarfs barely change over a Hubble time. While these evolutionary effects are taken into account in theoretical models, the lack of reliable age measurements for M dwarfs has prevented any detailed investigation of the consistency of these models over a wide range of ages. A difference in the measured overinflation of young and old M dwarfs could help reveal why evolutionary models consistently underpredict the radii of low-mass stars.

Fig. 8 shows the overinflation of M dwarfs as a function of their total age (where the overinflation is measured using the nearest model in age). The white dwarf plus M dwarf binaries clearly cover a wide age range. However, there is no clear indication of more or less overinflation as a function of age. More objects with reliable age

[2] https://github.com/awmann/M_-M_K-

Downloaded from https://academic.oup.com/mnras/article/481/1/1083/5079656 by guest on 18 November 2024

measurements, particularly old objects (>7 Gyr), will be needed to test this more robustly.

4.6 The effect of metallicity

Metallicity is expected to have a small but noticeable impact on the radius of a low-mass star. Lower metallicities lead to decreased opacity of the outer layers of the star and hence decreased radiation pressure, resulting in a smaller star (e.g. Chabrier & Baraffe 1997). For example, for the theoretical models of Dotter et al. (2008), the difference in radius between a 0.2 $M_{\odot}$ star with [Fe/H] = –1.0 and [Fe/H] = +0.5 is 9 per cent, which is detectable given our precision.

Fig. 9 shows the overinflation of M dwarfs as a function of their metallicity. There is no clear evidence of metal-poor stars being smaller or metal-rich stars being larger in this plot. However, the vast majority of objects plotted in Fig. 9 have roughly solar metallicity and the extremes of metallicity are poorly sampled. For the white dwarf plus M dwarf systems this is primarily because we determined the metallicities using the semi-empirical method of Newton et al. (2014), which is only valid between –0.6 < [Fe/H] < 0.3. It is also worth noting that there has been some criticism of metallicity calibrators based on the spectral analysis of M dwarfs (e.g. Lindgren & Heiter 2017), so Fig. 9 should be interpreted with some caution.

4.7 The effect of rotation

The effects of rotation on the radii of low-mass stars were investigated in detail by Kraus et al. (2011), who found that M dwarfs in short period binaries ($P_{\rm orb}$ < 1 d) were more oversized than those in longer period systems. This is consistent with the theory that rapid rotation leads to enhanced magnetic activity which inhibits convection leading to inflation.

In Fig. 10 we plot the overinflation as a function of orbital period. Our new systems all occupy the very shortest period end, extending precision measurements to the shortest periods measured to date. While we expect the M stars in our binaries to be tidally locked to the white dwarf and hence have rotation periods equal to the orbital periods, that is not the case for many other types of binary, particularly those with periods longer than a few days. In these cases the stars generally rotate slower than the orbital period. Furthermore, our new binaries all have very circular orbits (for example the eccentricity of NN Ser has been constrained to $e < 10^{-3}$; Parsons et al. 2014), but many of the longer period main-sequence binaries have substantial eccentricities. These are listed in the Appendix.

In contrast to the results of Kraus et al. (2011), Fig. 10 shows little difference in the overinflation of low-mass stars rotating faster or slower than 1 day, although in both cases there is substantial scatter in the radii. However, at periods longer than roughly 5 days the measured radii do appear to be more consistent with theoretical predictions although they show a similar amount of scatter.

5 CONCLUSIONS

We have presented high-precision mass, radius, effective temperature and age measurements for 23 M dwarfs in eclipsing binaries with white dwarfs, 16 of which are new results. We have also determined the metallicities for 13 of these objects. On average the radii of these stars are 6.2 ± 4.8 per cent larger than theoretical models predict, although they show a large amount of scatter, and around a quarter of them have measured radii consistent with models. No difference is seen between partially and fully convective stars. The fact that all of these stars are rapid rotators means that enhanced activity leading to the suppression of convection cannot be the only cause of the discrepancy in the radii of low-mass stars.

We find that the measured temperatures of very low mass M dwarfs (<0.2 $M_{\odot}$) are in agreement with theoretical models, but more massive stars are systematically cooler than models predict by ∼100 K.

Finally, we find no clear trend in the overinflation of M dwarfs as a function of age or metallicity, but do find that M dwarfs rotating slower than ∼5 days have on average radii more consistent with models, although there is a similar amount of scatter compared to more rapidly rotating M dwarfs.

The results presented in this paper demonstrate the difficulty in determining reliable parameters for low-mass stars and by extension any planets that they may host. The use of theoretical or empirical relations may still lead to errors of 5–10 per cent in the radii of exoplanets around M dwarfs, generally insufficient to constrain their internal structure and bulk composition.

ACKNOWLEDGEMENTS

SGP acknowledges the support of the Leverhulme Trust. The research leading to these results has received funding from the European Research Council under the European Union's Seventh Framework Programme (FP/2007-2013) / ERC Grant Agreement numbers 340040 (HiPERCAM) and 320964 (WDTracer). ULTRACAM, TRM, VSD, and SPL are supported by the Science and Technology Facilities Council (STFC). ARM acknowledges financial support from the MINECO Ramón y Cajal programme RYC-2016-20254 and the grant AYA2017-86274-P, and from the AGAUR (SGR-661/2017). Support for this work was provided by NASA through Hubble Fellowship grant *HST*-HF2-51357.001-A. MRS thanks for support from FONDECYT (1141269) and Millennium Science Initiative, Chilean ministry of Economy: Nucleus P10-022-F. MZ acknowledges support from CONICYT PAI (Concurso Nacional de Inserción en la Academia 2017, Folio 79170121) and CONICYT/FONDECYT (Programa de Iniciación, Folio 11170559). This work has made use of data obtained at the Thai National Observatory on Doi Inthanon, operated by NARIT. The results presented in this paper are based on observations collected at the European Southern Observatory under programme IDs 086.D-0161, 086.D-0265, 192.D-0270 and 099.D-0252.

REFERENCES

Allard F., Homeier D., Freytag B., Schaffenberger W., Rajpurohit A. S., 2013, Memorie della Societa Astronomica Italiana Supplementi, 24, 128
Anglada-Escudé G. et al., 2016, Nature, 536, 437
Bailer-Jones C. A. L., Rybizki J., Fouesneau M., Mantelet G., Andrae R., 2018, AJ, 156, 58
Ballard S., 2018, ApJ, preprint (arXiv:1801.04949)
Baraffe I., Chabrier G., Barman T. S., Allard F., Hauschildt P. H., 2003, A&A, 402, 701
Baraffe I., Homeier D., Allard F., Chabrier G., 2015, A&A, 577, A42
Barnes S. A., 2010, ApJ, 722, 222
Bayo A., Rodrigo C., Barrado Y Navascués D., Solano E., Gutiérrez R., Morales-Calderón M., Allard F., 2008, A&A, 492, 277
Beatty T. G. et al., 2007, ApJ, 663, 573
Berger D. H. et al., 2006, ApJ, 644, 475
Birkby J. et al., 2012, MNRAS, 426, 1507
Blake C. H., Torres G., Bloom J. S., Gaudi B. S., 2008, ApJ, 684, 635

Downloaded from https://academic.oup.com/mnras/article/481/1/1083/5079656 by guest on 18 November 2024

Carter J. A. et al., 2011, Science, 331, 562
Casewell S. L. et al., 2018, preprint (arXiv:1808.02761)
Catalán S., Isern J., García-Berro E., Ribas I., 2008, MNRAS, 387, 1693
Chabrier G., Baraffe I., 1997, A&A, 327, 1039
Charbonneau D. et al., 2009, Nature, 462, 891
Chaturvedi P., Sharma R., Chakraborty A., Anandarao B. G., Prasad N. J. S. S. V., 2018, AJ, 156, 27
Creevey O. L. et al., 2005, ApJ, 625, L127
Cruz P., Diaz M., Birkby J., Barrado D., Sipöcz B., Hodgkin S., 2018, MNRAS, 476, 5253
Delrez L. et al., 2018, in Society of Photo-Optical Instrumentation Engineers (SPIE) Conference Series., p. 107001I
Demory B.-O. et al., 2009, A&A, 505, 205
Dhillon V. S. et al., 2007, MNRAS, 378, 825
Dhillon V. S. et al., 2014, MNRAS, 444, 4009
Díaz R. F. et al., 2014, A&A, 572, A109
Dittmann J. A. et al., 2017a, Nature, 544, 333
Dittmann J. A. et al., 2017b, ApJ, 836, 124
Dorn C., Khan A., Heng K., Connolly J. A. D., Alibert Y., Benz W., Tackley P., 2015, A&A, 577, A83
Dotter A., Chaboyer B., Jevremović D., Kostov V., Baron E., Ferguson J. W., 2008, ApJS, 178, 89
Doyle L. R. et al., 2011, Science, 333, 1602
Eigmüller P. et al., 2016, AJ, 151, 84
Eigmüller P. et al., 2018, MNRAS,
Gaia Collaboration et al., 2018, A&A, 616, A1
Gillon M. et al., 2016, Nature, 533, 221
Gillon M. et al., 2017, Nature, 542, 456
Gómez Maqueo Chew Y. et al., 2014, A&A, 572, A50
Hardy L. K. et al., 2017, MNRAS, 465, 4968
Hartman J. D., Bakos G. Á., Noyes R. W., Sipőcz B., Kovács G., Mazeh T., Shporer A., Pál A., 2011, AJ, 141, 166
Hartman J. D. et al., 2018, AJ, 155, 114
Hebb L., Wyse R. F. G., Gilmore G., Holtzman J., 2006, AJ, 131, 555
Hełminiak K. G. et al., 2012, MNRAS, 425, 1245
Hjellming M. S., Taam R. E., 1991, ApJ, 370, 709
Iglesias-Marzoa R., López-Morales M., Arévalo M. J., Coughlin J. L., Lázaro C., 2017, A&A, 600, A55
Irwin J. et al., 2009, ApJ, 701, 1436
Irwin J. M. et al., 2011, ApJ, 742, 123
Jackson R. J., Deliyannis C. P., Jeffries R. D., 2018, MNRAS, 476, 3245
Kesseli A. Y., Muirhead P. S., Mann A. W., Mace G., 2018, AJ, 155, 225
Kopparapu R. k., Wolf E. T., Arney G., Batalha N. E., Haqq-Misra J., Grimm S. L., Heng K., 2017, ApJ, 845, 5
Kraus A. L., Tucker R. A., Thompson M. I., Craine E. R., Hillenbrand L. A., 2011, ApJ, 728, 48
Kraus A. L. et al., 2017, ApJ, 845, 72
Lindgren S., Heiter U., 2017, A&A, 604, A97
López-Morales M., 2007, ApJ, 660, 732
López-Morales M., Ribas I., 2005, ApJ, 631, 1120
Mann A. W., Gaidos E., Ansdell M., 2013, ApJ, 779, 188
Marsh T. R., Robinson E. L., Wood J. H., 1994, MNRAS, 266, 137
Morales J. C., Ribas I., Jordi C., 2008, A&A, 478, 507
Newton E. R., Charbonneau D., Irwin J., Berta-Thompson Z. K., Rojas-Ayala B., Covey K., Lloyd J. P., 2014, AJ, 147, 20
Nutzman P., Charbonneau D., 2008, PASP, 120, 317
Ofir A., Gandolfi D., Buchhave L., Lacy C. H. S., Hatzes A. P., Fridlund M., 2012, MNRAS, 423, L1
Orosz J. A. et al., 2012a, Science, 337, 1511
Orosz J. A. et al., 2012b, ApJ, 758, 87
Parsons S. G., Marsh T. R., Copperwheat C. M., Dhillon V. S., Littlefair S. P., Gänsicke B. T., Hickman R., 2010, MNRAS, 402, 2591
Parsons S. G. et al., 2012a, MNRAS, 419, 304
Parsons S. G. et al., 2012b, MNRAS, 420, 3281
Parsons S. G. et al., 2012c, MNRAS, 426, 1950
Parsons S. G. et al., 2014, MNRAS, 438, L91
Parsons S. G. et al., 2015, MNRAS, 449, 2194
Parsons S. G. et al., 2016, MNRAS, 458, 2793
Parsons S. G. et al., 2017, MNRAS, 470, 4473
Pecaut M. J., Mamajek E. E., 2013, ApJS, 208, 9
Pont F. et al., 2006, A&A, 447, 1035
Pyrzas S. et al., 2012, MNRAS, 419, 817
Rappaport S., Verbunt F., Joss P. C., 1983, ApJ, 275, 713
Rebassa-Mansergas A., Ren J. J., Parsons S. G., Gänsicke B. T., Schreiber M. R., García-Berro E., Liu X.-W., Koester D., 2016a, MNRAS, 458, 3808
Rebassa-Mansergas A. et al., 2016b, MNRAS, 463, 1137
Reiners A. et al., 2018, A&A, 612, A49
Ren J.-J., Rebassa-Mansergas A., Parsons S. G., Liu X.-W., Luo A.-L., Kong X., Zhang H.-T., 2018, MNRAS, 477, 4641
Ricker G. R. et al., 2015, J. Astron. Telescopes, Instrum. Syst., 1, 014003
Rogers L. A., Seager S., 2010, ApJ, 712, 974
Schwamb M. E. et al., 2013, ApJ, 768, 127
Seager S., 2013, Science, 340, 577
Serenelli A. M., Bergemann M., Ruchti G., Casagrande L., 2013, MNRAS, 429, 3645
Shporer A. et al., 2017, ApJ, 847, L18
Sirotkin F. V., Kim W.-T., 2010, ApJ, 721, 1356
Soderblom D. R., Duncan D. K., Johnson D. R. H., 1991, ApJ, 375, 722
Southworth J., Wheatley P. J., Sams G., 2007, MNRAS, 379, L11
Stassun K. G., Collins K. A., Gaudi B. S., 2017, AJ, 153, 136
Stassun K. G., Corsaro E., Pepper J. A., Gaudi B. S., 2018, AJ, 155, 22
Triaud A. H. M. J. et al., 2013, A&A, 549, A18
Vaccaro T. R., Rudkin M., Kawka A., Vennes S., Oswalt T. D., Silver I., Wood M., Smith J. A., 2007, ApJ, 661, 1112
Valencia D., Sasselov D. D., O'Connell R. J., 2007, ApJ, 665, 1413
Vernet J. et al., 2011, A&A, 536, A105
von Boetticher A. et al., 2017, A&A, 604, L6
Wandel A., 2018, ApJ, 856, 165
Welsh W. F. et al., 2015, ApJ, 809, 26
West A. A., Walkowicz L. M., Hawley S. L., 2005, PASP, 117, 706
Wheatley P. J. et al., 2018, MNRAS, 475, 4476
Zhou G. et al., 2015, MNRAS, 451, 2263
Zorotovic M., Schreiber M. R., Gänsicke B. T., 2011, A&A, 536, A42

APPENDIX A: A CATALOGUE OF WELL CHARACTERIZED M DWARFS

Downloaded from https://academic.oup.com/mnras/article/481/1/1083/5079656 by guest on 18 November 2024

Table A1. M dwarfs with well-constrained physical parameters. e is the eccentricity of the orbit. References: (1) Birkby et al. (2012), (2) Blake et al. (2008), (3) Carter et al. (2011), (4) Creevey et al. (2005), (5) Hartman et al. (2011), (6) Hebb et al. (2006), (7) Hełminiak et al. (2012), (8) Irwin et al. (2009), (9) Irwin et al. (2011), (10) Kraus et al. (2011), (11) López-Morales (2007), (12) Vaccaro et al. (2007), (13) Zhou et al. (2015), (14) Dittmann et al. (2017b), (15) Hartman et al. (2018), (16) Kraus et al. (2017), (17) Cruz et al. (2018), (18) Casewell et al. (2018), (19) Doyle et al. (2011), (20) Orosz et al. (2012b), (21) Orosz et al. (2012a), (22) Schwamb et al. (2013), (23) Welsh et al. (2015), (24) Pont et al. (2006), (25) Beatty et al. (2007), (26) Díaz et al. (2014), (27) Shporer et al. (2017), (28) Chaturvedi et al. (2018), (29) Ofir et al. (2012), (30) Gómez Maqueo Chew et al. (2014), (31) Eigmüller et al. (2016), (32) Iglesias-Marzoa et al. (2017), (33) von Boetticher et al. (2017), (34) Triaud et al. (2013), (35) Eigmüller et al. (2018), (36) Mann, Gaidos & Ansdell (2013).

Name	Mass ($M_\odot$)	Radius ($R_\odot$)	$T_{\rm eff}$ (K)	[Fe/H] (dex)	Age (Gyr)	Sp type	$P_{\rm orb}$ (d)	e	Ref
Double lined eclipsing binaries:									
19b-2-01387a	0.498 ± 0.019	0.496 ± 0.013	3498 ± 100	-	-	M2.7 ± 0.5	1.4985	0.01	1
19b-2-01387b	0.481 ± 0.017	0.479 ± 0.013	3436 ± 100	-	-	-	1.4985	0.01	1
19c-3-01405a	0.410 ± 0.023	0.398 ± 0.019	3309 ± 130	-	-	M2.8 ± 0.5	4.9391	0.01	1
19c-3-01405b	0.376 ± 0.024	0.393 ± 0.019	3305 ± 130	-	-	-	4.9391	0.01	1
19e-3-08413a	0.463 ± 0.025	0.480 ± 0.022	3506 ± 140	-	-	M2.3 ± 0.5	1.6734	0.01	1
19e-3-08413b	0.351 ± 0.019	0.375 ± 0.020	3338 ± 140	-	-	-	1.6734	0.01	1
SDSS J0318-0100a	0.272 ± 0.020	0.268 ± 0.010	3320 ± 130	-	-	-	0.4070	0.00	2
SDSS J0318-0100b	0.240 ± 0.022	0.248 ± 0.009	3300 ± 130	-	-	-	0.4070	0.00	2
KOI-126a	0.2413 ± 0.0030	0.2543 ± 0.0014	3300 ± 150	+0.15 ± 0.08	4.0 ± 1.0	-	1.7671	0.02	3
KOI-126b	0.2127 ± 0.0026	0.2318 ± 0.0013	3200 ± 150	+0.15 ± 0.08	4.0 ± 1.0	-	1.7671	0.02	3
TrES-Her0-07621a	0.493 ± 0.003	0.453 ± 0.060	3500 ± 150	-	-	M3.0 ± 1.0	1.1208	0.00	4
TrES-Her0-07621b	0.489 ± 0.003	0.452 ± 0.050	3395 ± 150	-	-	M3.0 ± 1.0	1.1208	0.00	4
1RXS J1547+4508a	0.2576 ± 0.0085	0.2895 ± 0.0068	-	-	-	-	3.5500	0.00	5
1RXS J1547+4508b	0.2585 ± 0.0080	0.2895 ± 0.0068	-	-	-	-	3.5500	0.00	5
2MASS J0446+1901a	0.470 ± 0.050	0.570 ± 0.020	3320 ± 150	-	0.15 ± 0.05	M2.5 ± 0.5	0.6188	0.00	6
2MASS J0446+1901b	0.190 ± 0.020	0.210 ± 0.010	2900 ± 150	-	0.15 ± 0.05	-	0.6188	0.00	6
ASAS J0113-3821a	0.612 ± 0.030	0.596 ± 0.020	3750 ± 250	-	-	-	0.4456	0.00	7
ASAS J0113-3821b	0.445 ± 0.019	0.445 ± 0.024	3085 ± 300	-	-	-	0.4456	0.00	7
GJ 3236a	0.376 ± 0.017	0.3828 ± 0.0072	3313 ± 110	-	-	-	0.7713	0.00	8
GJ 3236b	0.281 ± 0.015	0.2992 ± 0.0075	3238 ± 108	-	-	-	0.7713	0.00	8
LSPM J1112+7626a	0.3946 ± 0.0023	0.3860 ± 0.0054	3061 ± 162	-	-	-	41.032	0.24	9
LSPM J1112+7626b	0.2745 ± 0.0012	0.2978 ± 0.0047	2952 ± 163	-	-	-	41.032	0.24	9
MG1-78457a	0.527 ± 0.002	0.505 ± 0.008	3330 ± 60	-	-	-	1.5862	0.00	10
MG1-78457b	0.491 ± 0.001	0.471 ± 0.009	3270 ± 60	-	-	-	1.5862	0.00	10
MG1-116309a	0.567 ± 0.002	0.552 ± 0.013	3920 ± 80	-	-	-	0.8271	0.00	10
MG1-116309b	0.532 ± 0.002	0.532 ± 0.008	3810 ± 80	-	-	-	0.8271	0.00	10
MG1-506664a	0.584 ± 0.002	0.560 ± 0.004	3730 ± 90	-	-	-	1.5485	0.00	10
MG1-506664b	0.544 ± 0.002	0.513 ± 0.008	3610 ± 90	-	-	-	1.5485	0.00	10
MG1-646680a	0.499 ± 0.002	0.457 ± 0.006	3730 ± 20	-	-	-	1.6375	0.00	10
MG1-646680b	0.443 ± 0.002	0.427 ± 0.006	3630 ± 20	-	-	-	1.6375	0.00	10
MG1-1819499a	0.557 ± 0.001	0.569 ± 0.023	3690 ± 80	-	-	-	0.6303	0.00	10
MG1-1819499b	0.535 ± 0.001	0.500 ± 0.014	3610 ± 80	-	-	-	0.6303	0.00	10
MG1-2056316a	0.469 ± 0.002	0.441 ± 0.002	3460 ± 180	-	-	-	1.7228	0.00	10
MG1-2056316b	0.382 ± 0.001	0.374 ± 0.002	3320 ± 180	-	-	-	1.7228	0.00	10
CM Dra a	0.2307 ± 0.0010	0.2516 ± 0.0020	3360 ± 100	−0.67 ± 0.20	4.10 ± 0.80	M4.5	1.2684	0.01	11
CM Dra b	0.2136 ± 0.0001	0.2347 ± 0.0019	3320 ± 100	−0.67 ± 0.20	4.10 ± 0.80	M4.5	1.2684	0.01	11
YY Gem a	0.5992 ± 0.0047	0.6191 ± 0.0057	3820 ± 100	+0.10 ± 0.20	0.32 ± 0.08	M0.5 ± 0.5	0.8143	0.00	11
YY Gem b	0.5992 ± 0.0047	0.6191 ± 0.0057	3820 ± 100	+0.10 ± 0.20	0.32 ± 0.08	M0.5 ± 0.5	0.8143	0.00	11
CU Cnc a	0.4333 ± 0.0017	0.4317 ± 0.0052	3160 ± 150	-	0.32 ± 0.08	M3.5 ± 0.5	2.7715	0.00	11
CU Cnc b	0.3980 ± 0.0014	0.3908 ± 0.0094	3125 ± 150	-	0.32 ± 0.08	M3.5 ± 0.5	2.7715	0.00	11
GU Boo a	0.610 ± 0.007	0.623 ± 0.016	3920 ± 130	-	-	-	0.4887	0.00	11
GU Boo b	0.599 ± 0.006	0.620 ± 0.020	3810 ± 130	-	-	-	0.4887	0.00	11
OGLE BW3 V38a	0.44 ± 0.07	0.51 ± 0.04	3500 ± 200	-	-	M3.0 ± 1.0	0.1984	0.00	11
OGLE BW3 V38b	0.41 ± 0.09	0.44 ± 0.06	3448 ± 200	-	-	-	0.1984	0.00	11
TRES-Her0-07621a	0.493 ± 0.003	0.453 ± 0.060	3500 ± 200	-	-	M3.0 ± 1.0	1.1208	0.00	11
TRES-Her0-07621b	0.489 ± 0.003	0.452 ± 0.050	3395 ± 200	-	-	M3.0 ± 1.0	1.1208	0.00	11
UNSW-TR 2a	0.529 ± 0.035	0.641 ± 0.050	-	-	-	-	2.1167	0.00	11
UNSW-TR 2b	0.512 ± 0.035	0.608 ± 0.060	-	-	-	-	2.1167	0.00	11
LP 133-373a	0.340 ± 0.014	0.33 ± 0.02	3058 ± 195	-	>3.0	M4.5 ± 0.5	1.6280	0.00	12
LP 133-373b	0.340 ± 0.014	0.33 ± 0.02	3144 ± 206	-	>3.0	M4.5 ± 0.5	1.6280	0.00	12
HATS551-027a	0.2440 ± 0.0030	0.2610 ± 0.0075	3190 ± 100	+0.00 ± 0.20	-	-	4.0770	0.00	13
HATS551-027b	0.1790 ± 0.0015	0.2180 ± 0.0100	2990 ± 110	+0.00 ± 0.20	-	-	4.0770	0.00	13
LP 661-13a	0.3080 ± 0.0008	0.3226 ± 0.0033	-	−0.07 ± 0.20	-	M3.5 ± 0.5	4.7044	0.00	14
LP 661-13b	0.1940 ± 0.0003	0.2174 ± 0.0023	-	−0.07 ± 0.20	-	M4.3 ± 0.5	4.7044	0.00	14

Downloaded from https://academic.oup.com/mnras/article/481/1/1083/5079656 by guest on 18 November 2024

Table A1 – *continued*

Name	Mass ($M_\odot$)	Radius ($R_\odot$)	$T_{\rm eff}$ (K)	[Fe/H] (dex)	Age (Gyr)	Sp type	$P_{\rm orb}$ (d)	e	Ref
HAT-TR-318-007a	0.4480 ± 0.0110	0.4548 ± 0.0036	3190 ± 110	$+0.30 \pm 0.08$	-	M3.7 ± 0.7	3.3440	0.01	15
HAT-TR-318-007b	0.2721 ± 0.0042	0.2913 ± 0.0024	3100 ± 110	$+0.30 \pm 0.08$	-	M5.0 ± 0.7	3.3440	0.01	15
PTFEB 132+19a	0.3953 ± 0.0020	0.363 ± 0.008	3260 ± 90	$+0.14 \pm 0.04$	$0.60 - 0.80$	-	6.0157	0.00	16
PTFEB 132+19b	0.2098 ± 0.0014	0.272 ± 0.012	3120 ± 110	$+0.14 \pm 0.04$	$0.60 - 0.80$	-	6.0157	0.00	16
17e-3-02003a	0.597 ± 0.020	0.611 ± 0.095	3800 ± 100	-	-	0.0 ± 0.5	1.2250	0.00	17
17e-3-02003b	0.510 ± 0.016	0.540 ± 0.110	3500 ± 100	-	-	2.5 ± 0.5	1.2250	0.00	17
17h-4-01429a	0.503 ± 0.016	0.514 ± 0.006	3400 ± 100	-	-	3.0 ± 0.5	1.4446	0.00	17
17h-4-01429b	0.409 ± 0.013	0.421 ± 0.006	3200 ± 100	-	-	4.0 ± 0.5	1.4446	0.00	17
19c-3-08647a	0.393 ± 0.019	0.494 ± 0.069	3900 ± 100	-	-	M0.0 ± 0.5	0.8675	0.00	17
19c-3-08647b	0.244 ± 0.014	0.422 ± 0.077	3000 ± 100	-	-	M5.0 ± 0.5	0.8675	0.00	17
19f-4-05194a	0.531 ± 0.016	0.651 ± 0.007	4400 ± 100	-	-	-	0.5895	0.00	17
19f-4-05194b	0.385 ± 0.011	0.425 ± 0.006	3500 ± 100	-	-	M2.5 ± 0.5	0.5895	0.00	17
NGTS J0522-2507a	0.1739 ± 0.0015	0.2045 ± 0.0058	2995 ± 100	-	-	M5.0 ± 1.0	1.7477	0.00	18
NGTS J0522-2507b	0.1742 ± 0.0019	0.2168 ± 0.0048	2997 ± 100	-	-	M5.0 ± 1.0	1.7477	0.00	18
Kepler-16B	0.2026 ± 0.0007	0.2262 ± 0.0006	-	-0.30 ± 0.20	-	-	41.0792	0.16	19
Kepler-38B	0.249 ± 0.010	0.2724 ± 0.0050	-	-	-	-	18.7953	0.10	20
Kepler-47B	0.362 ± 0.013	0.3506 ± 0.0063	3357 ± 100	-	-	-	7.4484	0.02	21
PH1B	0.378 ± 0.023	0.408 ± 0.024	-	-	-	-	20.0003	0.22	22
Kepler-453B	0.195 ± 0.002	0.2150 ± 0.0014	3226 ± 100	-	-	-	27.3220	0.05	23
Secondaries in eclipsing binaries:									
OGLE-TR 5b	0.271 ± 0.035	0.263 ± 0.012	-	-	-	-	0.8083	0.00	11
OGLE-TR 6b	0.359 ± 0.025	0.393 ± 0.018	-	-	-	-	4.5488	0.00	11
OGLE-TR 7b	0.281 ± 0.029	0.282 ± 0.013	-	-	-	-	2.7182	0.00	11
OGLE-TR 18b	0.387 ± 0.049	0.39 ± 0.04	-	-	-	-	2.2280	0.00	11
OGLE-TR 34b	0.509 ± 0.038	0.435 ± 0.033	-	$+0.32 \pm 0.31$	-	-	8.5763	0.00	11
OGLE-TR 78b	0.243 ± 0.015	0.240 ± 0.013	-	-	-	-	5.3187	0.12	11
OGLE-TR 106b	0.116 ± 0.021	0.181 ± 0.013	-	-	-	-	2.5359	0.00	11
OGLE-TR 120b	0.47 ± 0.04	0.42 ± 0.02	-	-	-	-	9.1662	0.36	11
OGLE-TR 122b	0.092 ± 0.009	0.120 ± 0.019	-	$+0.15 \pm 0.36$	-	-	7.2695	0.23	11
OGLE-TR 123b	0.085 ± 0.011	0.133 ± 0.009	-	-	-	-	1.8039	0.00	24
OGLE-TR 125b	0.209 ± 0.033	0.211 ± 0.027	-	-	-	-	5.3039	0.00	11
HAT-TR-205-013b	0.124 ± 0.010	0.167 ± 0.006	-	-0.20 ± 0.50	-	-	2.2307	0.01	25
KOI-189b	0.0745 ± 0.0033	0.1025 ± 0.0024	-	-0.12 ± 0.10	$6.9^{+6.4}_{-3.4}$	-	30.360	0.28	26
KOI-686b	0.0987 ± 0.0049	0.1250 ± 0.0038	-	-0.06 ± 0.13	6.20 ± 2.80	-	52.514	0.56	26
EPIC 202900527b	0.1459 ± 0.0030	0.1702 ± 0.0046	-	$+0.32 \pm 0.04$	$8.49^{+0.97}_{-1.35}$	-	13.009	0.38	27
EPIC 206155547b	0.1612 ± 0.0070	0.1996 ± 0.0119	-	-0.32 ± 0.04	$10.4^{+1.2}_{-1.0}$	-	24.388	0.36	27
EPIC 206432863b	0.0942 ± 0.0019	0.0913 ± 0.0048	-	$+0.01 \pm 0.04$	$9.16^{+0.93}_{-0.91}$	-	11.990	0.26	27
SAO 106989b	0.256 ± 0.005	0.326 ± 0.012	2380 ± 260	-0.20 ± 0.10	~ 2.0	-	4.3979	0.25	28
HD 24465b	0.233 ± 0.002	0.244 ± 0.001	2335 ± 10	$+0.30 \pm 0.15$	~ 2.3	-	7.1963	0.21	28
EPIC 211682657b	0.599 ± 0.017	0.566 ± 0.005	4329 ± 50	-0.10 ± 0.15	~ 1.4	-	3.1420	0.01	28
HD 205403b	0.406 ± 0.005	0.444 ± 0.014	4651 ± 120	-0.10 ± 0.15	~ 1.2	-	2.4449	0.00	28
KIC 1571511b	0.1414 ± 0.0004	0.1783 ± 0.0006	4100 ± 50	-	-	-	14.0225	0.33	29
1SWASP J0113+3149	0.186 ± 0.010	0.209 ± 0.011	3922 ± 42	-0.40 ± 0.04	9.5 ± 1.0	-	14.2769	0.31	30
UCAC4 714-021661b	0.188 ± 0.014	0.234 ± 0.009	-	-0.05 ± 0.17	-	-	1.3512	0.07	31
T-Cyg1-12664b	0.376 ± 0.017	0.3475 ± 0.0081	3460 ± 210	-	-	M3.0	4.1288	0.04	32
EBLM J0555-57Ab	$0.0813^{+0.0038}_{-0.0037}$	$0.084^{+0.014}_{-0.004}$	-	-0.24 ± 0.16	-	-	7.7577	0.09	33
TYC 7760-484-1b	0.091 ± 0.002	0.117 ± 0.006	-	-0.21 ± 0.07	$6 - 12$	-	6.7600	0.06	34
EPIC 219654213	$0.187^{+0.012}_{-0.013}$	$0.200^{+0.007}_{-0.008}$	-	-0.08 ± 0.09	4.1 ± 1.1	M5.0	5.4420	0.01	35
Single stars:									
GJ 15A	0.405 ± 0.041	0.3863 ± 0.0021	3602 ± 13	-0.30 ± 0.07	-	M1.5 ± 0.5	-	-	36
GJ 205	0.637 ± 0.064	0.5735 ± 0.0044	3850 ± 22	$+0.49 \pm 0.07$	-	M0.0 ± 1.0	-	-	36
GJ 380	0.711 ± 0.071	0.6398 ± 0.0046	4176 ± 19	$+0.24 \pm 0.07$	-	-	-	-	36
GJ 526	0.490 ± 0.049	0.4840 ± 0.0084	3646 ± 34	-0.31 ± 0.07	-	M1.5 ± 0.5	-	-	36
GJ 687	0.403 ± 0.040	0.4183 ± 0.0070	3457 ± 35	-0.05 ± 0.07	-	M3.0 ± 0.5	-	-	36
GJ 880	0.572 ± 0.057	0.5477 ± 0.0048	3731 ± 16	$+0.21 \pm 0.07$	-	M1.5 ± 0.5	-	-	36
GJ 887	0.494 ± 0.049	0.4712 ± 0.0086	3695 ± 35	-0.06 ± 0.07	-	M2.0 ± 1.0	-	-	36
GJ 699	0.159 ± 0.016	0.1869 ± 0.0012	3238 ± 11	-0.40 ± 0.07	-	M4.0	-	-	36
GJ 411	0.392 ± 0.039	0.3924 ± 0.0033	3532 ± 17	-0.38 ± 0.07	-	M2.0	-	-	36
GJ 105A	0.767 ± 0.124	0.7949 ± 0.0062	4704 ± 21	-0.28 ± 0.07	-	-	-	-	36
GJ 338A	0.630 ± 0.063	0.5773 ± 0.0131	3953 ± 41	-0.01 ± 0.07	-	-	-	-	36
GJ 338B	0.617 ± 0.062	0.5673 ± 0.0137	3926 ± 37	-0.04 ± 0.07	-	-	-	-	36
GJ 412A	0.390 ± 0.039	0.3982 ± 0.0091	3537 ± 41	-0.37 ± 0.07	-	M2.0	-	-	36
GJ 436	0.447 ± 0.045	0.4546 ± 0.0182	3520 ± 66	$+0.01 \pm 0.07$	-	M2.5 ± 0.5	-	-	36

Downloaded from https://academic.oup.com/mnras/article/481/1/1083/5079656 by guest on 18 November 2024

Table A1 *– continued*

Name	Mass ($M_\odot$)	Radius ($R_\odot$)	$T_{\rm eff}$ (K)	[Fe/H] (dex)	Age (Gyr)	Sp type	$P_{\rm orb}$ (d)	e	Ref
GJ 570A	0.740 ± 0.119	0.7390 ± 0.0190	4588 ± 58	-0.06 ± 0.07	-	-	-	-	36
GJ 581	0.308 ± 0.031	0.2990 ± 0.0100	3487 ± 62	-0.15 ± 0.07	-	M3.0	-	-	36
GJ 702B	0.749 ± 0.075	0.6697 ± 0.0089	4475 ± 33	$+0.01 \pm 0.07$	-	-	-	-	36
GJ 752A	0.330 ± 0.033	0.3561 ± 0.0039	3417 ± 17	-0.23 ± 0.07	-	$M3.0 \pm 0.5$	-	-	36
GJ 809	0.573 ± 0.057	0.5472 ± 0.0067	3744 ± 24	-0.06 ± 0.07	-	$M1.0 \pm 1.0$	-	-	36
GJ 820A	0.727 ± 0.073	0.6611 ± 0.0048	4399 ± 16	-0.27 ± 0.07	-	-	-	-	36
GJ 820B	0.656 ± 0.066	0.6010 ± 0.0072	4025 ± 24	-0.22 ± 0.07	-	-	-	-	36
GJ 892	0.771 ± 0.124	0.7784 ± 0.0053	4773 ± 20	-0.23 ± 0.07	-	-	-	-	36
GJ 514	0.526 ± 0.053	0.611 ± 0.043	3377 ± 100	-0.24 ± 0.20	-	$M1.0 \pm 1.0$	-	-	11
GJ 191	0.281 ± 0.014	0.291 ± 0.025	3570 ± 156	-0.90 ± 0.20	-	$M3.5 \pm 1.0$	-	-	11
GJ 551	0.123 ± 0.006	0.145 ± 0.011	3042 ± 117	-	-	$M5.5 \pm 0.5$	-	-	11

This paper has been typeset from a TEX/LATEX file prepared by the author.

Downloaded from https://academic.oup.com/mnras/article/481/1/1083/5079656 by guest on 18 November 2024